Prospective White-light Imaging and In Situ Measurements of Quiescent Large-scale Solar-wind Streams from the *Parker Solar Probe* and *Solar Orbiter*

Ming Xiong[1,2,3] , Jackie A. Davies[4] , Xueshang Feng[1,2] , Bo Li[5] , Liping Yang[1,2] , Lidong Xia[5] , Richard A. Harrison[4] , Keiji Hayashi[1,6] , Huichao Li[1,3] , and Yufen Zhou[1,2]

[1] State Key Laboratory of Space Weather, National Space Science Center, Chinese Academy of Sciences, Beijing, People's Republic of China; mxiong@swl.ac.cn
[2] HIT Institute of Space Science and Applied Technology, Shenzhen, People's Republic of China
[3] University of Chinese Academy of Sciences, Beijing, People's Republic of China
[4] RAL Space, STFC-Rutherford Appleton Laboratory, Harwell Campus, Didcot, UK
[5] Shandong Provincial Key Laboratory of Optical Astronomy and Solar-Terrestrial Environment, Institute of Space Sciences, Shandong University, Weihai, People's Republic of China
[6] Institute for Space-Earth Environmental Research, Nagoya University, Japan

Abstract

Deep-space exploration of the inner heliosphere is in an unprecedented golden age, with the recent and forthcoming launches of the *Parker Solar Probe* (*PSP*) and *Solar Orbiter* (*SolO*) missions, respectively. In order to both predict and understand the prospective observations by *PSP* and *SolO*, we perform forward MHD modeling of the 3D inner heliosphere at solar minimum, and synthesize the white-light (WL) emission that would result from Thomson scattering of sunlight from the coronal and heliospheric plasmas. Both solar rotation and spacecraft trajectory should be considered when reconstructing quiescent large-scale solar-wind streams from *PSP* and *SolO* WL observations. When transformed from a static coordinate system into a corotating one, the elliptical orbit of *PSP* becomes a multiwinding spiral. The innermost spiral winding of this corotating *PSP* orbit takes the form of a closed "heart shape" within around $80\,R_\odot$ of the Sun. *PSP*, when traveling along this "heart-shaped" trajectory, can cross a single corotating interaction region (CIR) twice. This enables in situ measurements of the same CIR to be made in both the corona and heliosphere. As *PSP* approaches perihelion, the WL radiance from the corona increases. Polarization can be used to localize the main WL scattering region in the corona. Large-scale structures around *PSP* can be further resolved in the longitudinal dimension, using additional WL imagery from the out-of-ecliptic perspective of *SolO*. Coordinated observations between *PSP* and *SolO* are very promising in the quest to differentiate background CIRs from transient ejecta.

Key words: magnetohydrodynamics (MHD) – methods: numerical – solar wind – Sun: corona – Sun: heliosphere

1. Introduction

The solar wind, ubiquitous in interplanetary space, links the Sun, Earth, and other solar system bodies to form a closely coupled system: the heliosphere. The solar wind, the supersonic and super-Alfvénic outflow of plasma from the upper solar atmosphere, extends far beyond the orbits of the outermost planets, terminating at the heliopause surrounded by the weakly ionized interstellar medium. The Alfvén surface (Schwadron et al. 2010; DeForest et al. 2014) is defined as the three-dimensional (3D) connection of Alfvén points, where the flow speed equals the Alfvén speed. The heliocentric distance of the Alfvén surface lies between 10 and 30 solar radii ($R_\odot$) of the Sun, as indicated by inbound waves in the visible corona (DeForest et al. 2014). The Alfvén surface and the heliopause (Holzer 1989; Suess 1990) delimit the inner and outer boundaries of the heliosphere. The solar wind originates from funnel-shaped structures rooted in the lanes of the magnetic network above the surface of the Sun (Tu et al. 2005). Within $2-3\,R_\odot$, the Sun's magnetic field tends to rotate with the Sun, but at larger distances the field stretches into interplanetary space with the supersonic solar wind flow. The imaginary surface between 2 and $3\,R_\odot$, where the solar magnetic field begins to radially expand, is termed as the solar source surface. The quasistationary solar wind has two modes, slow and fast, which are linked to origins near coronal streamers and coronal holes, respectively. The fast solar wind accelerates to speeds of $\sim 800\,\mathrm{km\,s^{-1}}$ within $10\,R_\odot$ of the Sun. The slow solar wind accelerates within the first $20\,R_\odot$ to speeds near $300\,\mathrm{km\,s^{-1}}$. Solar wind density correlates inversely with speed so that fast streams are associated with low density, and slow streams with high density. The energy flux density in fast streams roughly equals that in slow streams (Leer & Holzer 1980; Leer et al. 1982; Cranmer et al. 2017); the energy flux in dense slow streams acts predominantly to lift the solar wind mass out of the Sun's gravitational field, while the energy flux in the more rarefied fast streams mostly accelerates the particles to high speeds. At times, high-speed streams from coronal holes expand into, and overtake, the slow flow regions that mainly emerge near the ecliptic plane, thus allowing the slow and fast streams to interact. The resulting compression regions plow through the radially outward flowing ambient solar wind plasma. Such compression-rarefaction zones develop into corotating interaction regions (CIRs; Gosling et al. 1993). The quiescent solar wind can be considered as an interplanetary conduit for transient coronal mass ejections (CMEs). In contrast to a mass-loss rate of 10^9 kg per second due to the ambient solar wind, a typical CME carries a mass of 10^{13} kg of plasma out into the heliosphere (e.g., Gosling 1990; Webb & Howard 1994).

Particle and field detectors provide in situ measurements of the solar wind with a high temporal resolution, including solar wind speed, mass flux, composition, charge state, and magnetic

field. Such detailed continuous in situ measurements can be used to identify fine-scale solar wind structures, to diagnose solar wind turbulence from magnetohydrodynamic (MHD) to kinetic scales, and to test wave–particle interaction hypotheses. In 1962, proof of persistent solar wind flows and recurrent CIRs came as the *Mariner* II spacecraft probed interplanetary space on its flight to and past Venus (Neugebauer & Snyder 1966, 1967). The *Helios* and *Voyager* spacecraft sampled near to the Sun and far from it, respectively: *Helios* to within 0.3 au, and *Voyager* to 100 au and beyond. The *Ulysses* spacecraft sampled out of the ecliptic (OOE) plane enabled by a Jovian swing-by, reaching an orbital inclination of 80°. To date, *Ulysses*, albeit without any imaging instrumentation, is the only successful OOE mission to orbit the Sun, and has enabled study of the solar wind at almost all latitudes (Wenzel et al. 1992; Smith et al. 1995; McComas et al. 2000). Since 1996, the *Advanced Composition Explorer* (*ACE*) satellite, orbiting the Lagrangian point L1, has provided nearly continuous monitoring of the solar wind plasma headed toward Earth (Stone et al. 1998). *Wind* (Lepping et al. 1995), *SOHO* (Domingo et al. 1995), and *DSCOVR* (Biesecker et al. 2015) constitute additional sources of L1 in situ measurements. These in situ data reveal that the solar wind is not only hot, tenuous, and magnetized, but also highly conducting, virtually collisionless, and supersonic. Heliospheric CIRs can be identified from their in situ particle and wave signatures (Borovsky & Denton 2010), such as a gradual increase in solar wind speed, and a sharp enhancement in plasma density and magnetic field. In situ measurements are of the utmost importance in providing the "ground truth" for remote-sensing methods.

White-light (WL) imagers can be used to image both the quasisteady flow and transient disturbances, such as CMEs, in the solar wind by observing visible sunlight scattered by electrons therein. The Thomson-scattered WL from the corona and heliosphere is routinely observed by coronagraphs and heliosphere imagers, respectively. CMEs were first discovered with the *OSO*-7 coronagraph in the early 1970s (Tousey 1973), and are now recognized as the dominant driver of severe space weather events. CMEs are traditionally defined as bright transients expelled through a coronagraph field of view (FOV) over a period of minutes to hours (Hundhausen 1993). The radiance (brightness) patterns of CMEs in WL coronagraph images reflect their electron density distribution near the plane of sky (POS; Billings 1966). WL imaging of the heliospheric, at large solar elongations, was first performed by the Solar Mass Ejection Imager (SMEI; Eyles et al. 2003) on board the *Coriolis* spacecraft, and subsequently by the heliospheric imagers (HI-1 and HI-2; Howard et al. 2008; Eyles et al. 2009) on board the twin *STEREO* spacecraft (Kaiser et al. 2008) and the Wide-field Imager for Solar PRobe (WISPR; Vourlidas et al. 2016) on board the *Parker Solar Probe* (*PSP*; Fox et al. 2016). The *STEREO* mission is comprised of two spacecraft, with one leading the Earth (*STEREO A*) and the other trailing behind the Earth (*STEREO B*) in its orbit. An extreme ultraviolet imager (EUVI: 1–1.7 $R_\odot$ in the POS), two coronagraphs (COR1: 1.5–4 $R_\odot$ and COR2: 2.5–15 $R_\odot$), and two heliospheric imagers (HI-1: 15–84 $R_\odot$ and HI-2: 66–318 $R_\odot$) constitute the Sun–Earth Connection Coronal and Heliospheric Investigation (SECCHI) instrument package on board each *STEREO* spacecraft. The SECCHI instruments have a broad and continuous FOV, covering the full corona and a large portion of the inner heliosphere. Using *STEREO*/SECCHI, CIRs and CMEs can be continuously tracked in WL, from the inner corona all the way out to 1 au and beyond

(e.g., Harrison et al. 2008; Rouillard et al. 2008; Sheeley et al. 2008; Davies et al. 2009; Davis et al. 2009; Liu et al. 2010; DeForest et al. 2013). Remote WL imaging of the corona and heliosphere, particularly from the stereoscopic perspective provided by *STEREO*/SECCHI, establishes a cause-and-effect connection between solar eruptions and disturbances observed at Earth, and provides a contextual link between detailed in situ measurements at Earth and the large-scale solar wind streams passing over the planet.

Our understanding of the corona and heliosphere is essentially constrained by contemporary capabilities in terms of in situ and remote-sensing observation. Remote-sensing observations of the corona and heliosphere are different in terms of observing at different wavelengths and from different viewing perspectives. WL detectability of CIRs and CMEs in the heliosphere depends on both their electron density distribution and viewing perspective, because of the Thomson-scattering geometry. Because of the *STEREO* spacecraft orbit within the ecliptic plane, the longitudinal dimension of CIRs and CMEs is mainly integrated in *STEREO*/HI imagery. The determination of CME kinematics, and propagation direction, in particular, is still riddled with uncertainties, particularly when viewed at large elongations (Vourlidas & Howard 2006; Howard & Tappin 2009; Davies et al. 2012; Howard & DeForest 2012; Xiong et al. 2013a, 2013b). Because of the effect of Thomson-scattering geometry, CMEs that propagate along the Sun–Earth line would be clearly imaged in WL from an OOE solar orbit as well as from the L4/L5 Lagrangian points. Deep-space exploration of the inner heliosphere is in an unprecedented golden age, with the recent and forthcoming launches of the *PSP* and *Solar Orbiter* (*SolO*; Muller et al. 2013) missions, respectively. Using multiple Venus gravity assists, *PSP* will plunge repeatedly within 10 solar radii ($R_\odot$) of the Sun center. WISPR is the sole imager on board *PSP*. The ecliptic-centered FOV of WISPR covers a range of elongation angles extending from 13°.5 to 108°, with a spatial resolution of 6.4 arcmin. The ram-side mounted WISPR instrument will image solar wind structures prior to their detection in situ, with increasing spatial resolution as they ascend from the Sun toward the spacecraft. The dependency of Thomson-scattering emission from coronal electrons on imaging geometry dictates that WISPR will be very sensitive to plasma close to the spacecraft in contrast to the situation that arises when imaging from an Earth-like orbit. WISPR will be the first "in situ" imager, providing a crucial link between the large-scale corona and in situ measurements. *SolO*, once launched (currently scheduled for February 2020), will progressively increase its orbital inclination above 30°. The orbital parameters of *SolO* are listed as perihelion 0.28 au, aphelion 0.8–0.9 au, maximum inclination >30°, and period 150 days. *SolO* hosts multiple remote-sensing instruments, including the Multi-element Telescope for Imaging and Spectroscopy (*METIS*) coronagraph, which images the corona in WL and ultraviolet (UV), and the WL heliospheric imager (*SolO*-HI). *SolO* is expected to achieve the first OOE imaging of the corona and heliosphere in WL and UV. A panoramic OOE view in WL would be highly beneficial for revealing the morphology and kinematics of CIRs and CMEs in the hitherto unresolved longitudinal dimension, and hence for monitoring the propagation and evolution of in-ecliptic CMEs for space weather operations (Xiong et al. 2017, 2018). Other proposed OOE mission concepts, following from *SolO*, but at an inclination larger than 30°, include the Solar

Polar Imager (*SPI*; Liewer et al. 2008), POLAR Investigation of the Sun (*POLARIS*; Appourchaux et al. 2009), SOLAR sail Investigation of the Sun (*SOLARIS*; Appourchaux et al. 2014), Solar Polar ORbit Telescope (*SPORT*; Wu et al. 2011; Xiong et al. 2016), and *InterHelioProbe* (Kuznetsov et al. 2016). In addition, the ecliptic L1, L4, and L5 Lagrangian points are recognized as crucial for routine observation of space weather. The Lagrangian points are stable or metastable, so placing spacecraft in orbit around these points is advantageous in terms of propellant usage. A spacecraft at L1 with imaging and in situ measurement capabilities, such as *SOHO*, can remotely monitor the solar disk and solar corona as well as measuring the solar wind upstream of Earth. Spacecraft at L4/L5 are able to perform side-on imaging of Earth-directed CMEs in order to improve estimation of their propagation speed and direction. The twin *STEREO* spacecraft, launched in 2006, were pathfinders for future L4/L5 missions (Akioka et al. 2005; Biesecker et al. 2008; Gopalswamy et al. 2011; Lavraud et al. 2016; Kraft et al. 2017). Utilizing concerted operation of two spacecraft at both L1 and L5 points, the recently proposed *Lagrangian* mission can enhance space weather monitoring to provide early warnings of potential electromagnetic threats to Earth (Kraft et al. 2017). Though each mission has its own specific scientific goals and promises great scientific/operational advances, taken together those missions that come to fruition on the same timescale will contribute to the great heliophysics observatory as a whole, enabling genuine 3D exploration of the Sun and the inner heliosphere.

True 3D exploration of the inner heliosphere would become feasible using coordinated observation from both remote-sensing and in situ instruments on board multiple spacecraft at different heliospheric locations (r, θ, φ). As implied above, *PSP* and *SolO* will accommodate both remote-sensing and in situ instruments, enter different previously unexplored domains of the inner heliosphere, and provide radically new observations of the Sun-heliosphere system. Prospective joint observations from *PSP* and *SolO* can be predicted on the basis of numerical forward MHD modeling, as demonstrated in our previous studies that synthesized the WL images of CIRs (Xiong et al. 2017) and CMEs (Xiong et al. 2018) that would be observed by a notional OOE spacecraft at 1 au. In the current paper, we use the numerical CESE-MHD model to simulate quiescent large-scale solar wind streams at solar minimum (Feng et al. 2010; Yang et al. 2012), use *Kepler*'s laws to calculate the *PSP* orbit around the Sun, and synthesize the Thomson-scattered WL emission from the corona and heliosphere that will be imaged by the in-ecliptic *PSP* and OOE *SolO* spacecraft. Section 2 presents the simulated 3D distribution of various solar wind parameters from corona to heliosphere. Section 3 investigates the in-ecliptic distribution of WL emission from CIRs. Section 4 presents predictions of the near-Sun signatures of CIRs that could be imaged in WL by the WISPR instrument on board *PSP* and measured by *PSP*'s in situ detectors. Section 5 demonstrates the benefit of the additional WL imaging from the OOE *SolO* spacecraft, in revealing the context of ambient structures near the in-ecliptic *PSP* spacecraft. Section 6 emphasizes the need for unification in the definition of the orbit of an interplanetary spacecraft and the design of WL imaging payload, and discusses the scientific merits of coordinated observations between *PSP* and *SolO* in 3D exploration of the inner heliosphere.

2. 3D Distribution of Solar Wind Streams from Corona to Heliosphere

The 3D solar wind streams in the corona and heliosphere during Carrington rotation CR2060 at solar minimum are numerically synthesized by prescribing synoptic photospheric magnetograms, and other solar observations, to define the inner boundary conditions at $r = 1\,R_\odot$ (Yang et al. 2012). The numerical solution gradually converges to a quiescent state through the time-dependent relaxation of the numerical CESE-MHD model (Feng et al. 2010). Furthermore, the initial inner boundary conditions at the photosphere are iteratively improved by checking the simulated local solar wind parameters against in situ measurements from *ACE* at the L1 point and *Ulysses* along its polar orbit. Various 2D cross-sections of the simulated solar wind density distribution during CR2060 are illustrated in Figure 1, while 3D isosurfaces of the density are shown in Figure 2. The coronal streamer belt, characterized by high-density confined plasma, lies within heliographic latitudes $\pm30°$ (Figures 1(a) and 2). Underneath the coronal streamer lies a photospheric polarity inversion line (PIL), as identified in the observed synoptic magnetogram. The smooth elliptical isosurface of coronal streamers at solar minimum (shown in Figure 2) is distorted into a highly irregular surface at solar maximum (Xiong et al. 2017). Coronal magnetic field lines inside coronal streamers are closed, while those outside coronal streamers are open. Accordingly, coronal plasma outside coronal streamers continuously escapes along open field lines into interplanetary space, such that the solar wind is super-Alfvénic within that regime. The solar wind outflow from the rotating Sun stretches the open coronal magnetic field lines into spiral interplanetary magnetic field lines. At solar minimum, the interplanetary solar wind is bimodal, with fast solar wind emerging at high latitudes and slow solar wind at low latitudes (Figure 1(f)). The slow solar wind is believed to be caused by magnetic interchange reconnection between the open and closed magnetic field lines on either side of the streamer boundaries (Abbo et al. 2016; Cranmer et al. 2017). The streamer belt astride a PIL generally does not align with the ecliptic equator, owing to the 7° difference between the magnetic and rotational axes of the Sun. Both fast and slow solar wind streams coexist within the ecliptic, and interplanetary compression between them forms three large-scale CIRs (Figures 1(e)–(f)). The density ridge on the spherical shells is continuous and diffuse at $r = 10\,R_\odot$, and detached and enhanced at $r = 215\,R_\odot$ (Figures 1(b)–(c)). The steepening of the radial compression region corresponding to each CIR is reproduced in our simulation.

3. In-ecliptic Distribution of WL Emission from CIRs

The WL imaging of the solar wind from WISPR is unprecedented for such an imaging instrument, due to the rapidly changing orbit and the very low perihelia of *PSP*. In contrast, all previous deep-space WL imaging payloads such as *SOHO*/LASCO and *STEREO*/SECCHI have been located near 1 au from the Sun. The effective resolution of WISPR for near-field objects will be better provided those objects can be resolved. As *PSP* rapidly approaches its perihelion, structures in the solar wind and corona streamers will be imaged with increasingly high resolution. Figure 3 presents the WL brightness, I, of the corona as imaged from different distances from the Sun, $r_{\mathrm{s/c}} = [215, 30, 20, 10]\,R_\odot$, along a
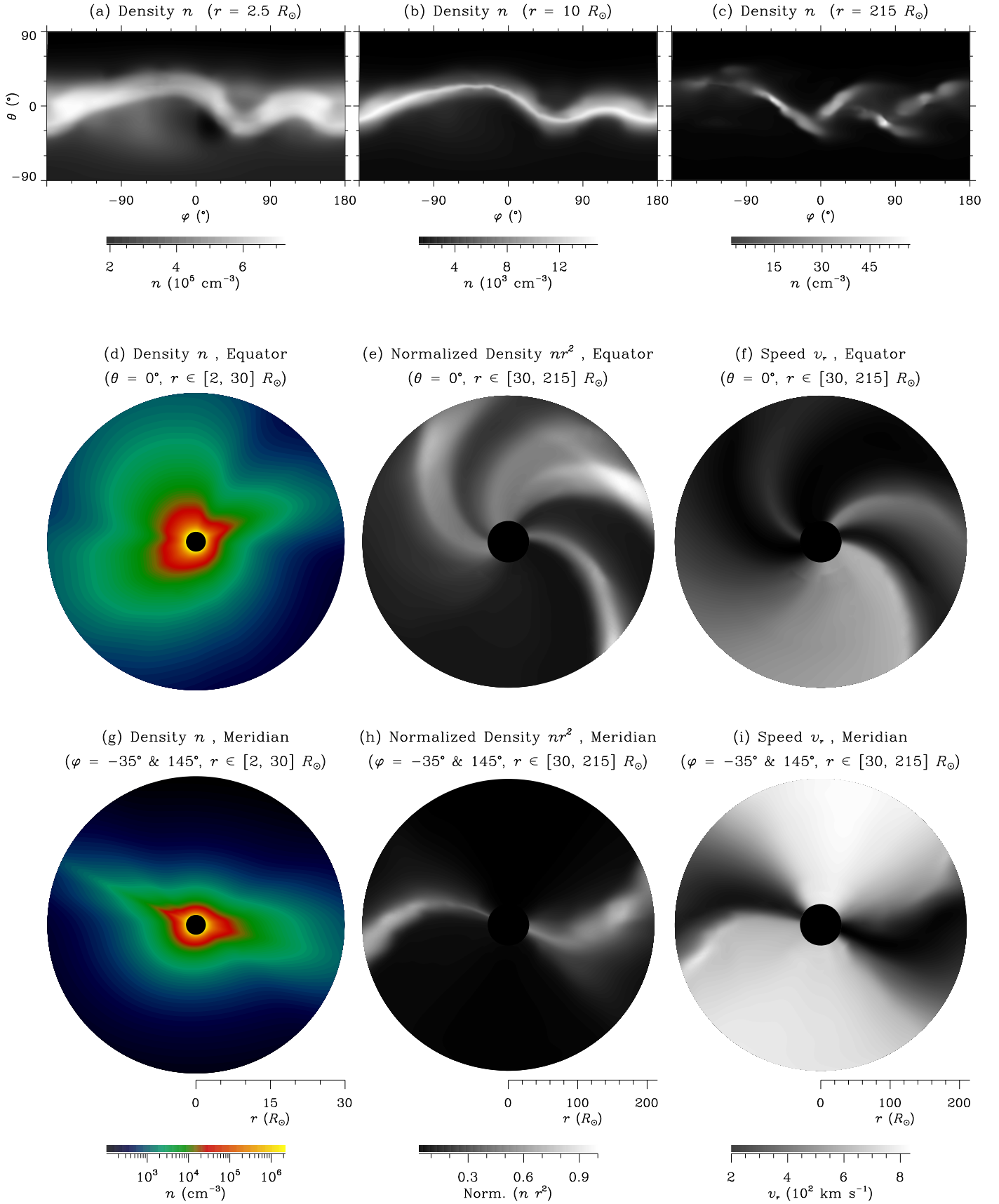
Figure 1. Distribution of the proton density, n, and radial speed, v_r, of the ambient solar wind, at various heliocentric distances (a)–(c), in the equator (d)–(f) and in a specified meridian (g)–(i), in the framework of a 3D geometry defined by radius, r, latitude, θ, and longitude, φ. Panels (a), (b), (d), and (g) are at coronal altitudes; panels (c), (e), (f), (h), and (i) are in the heliosphere. The heliospheric density, n, is normalized by $n\,r^2$ in panels (e) and (h).
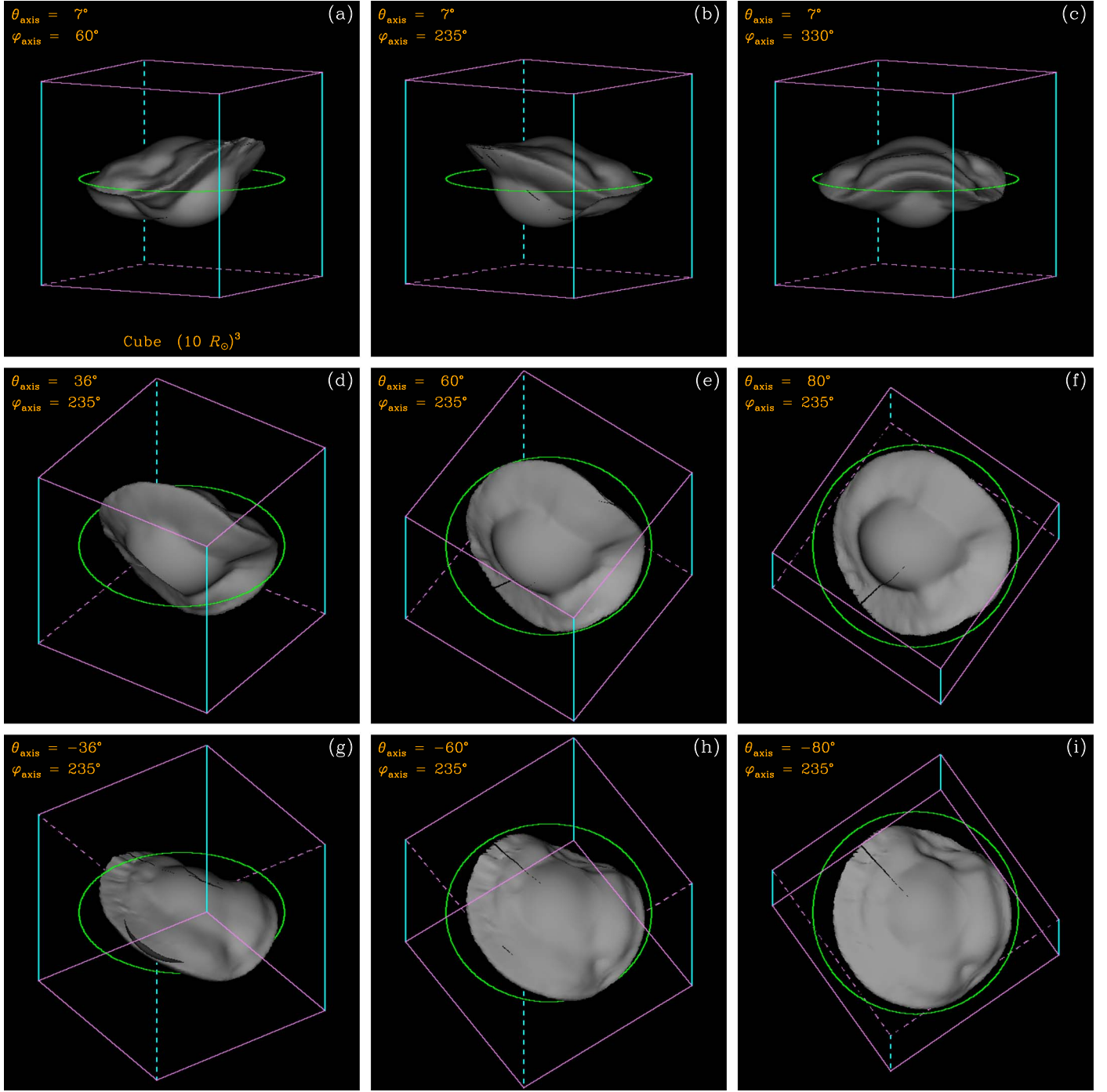
Figure 2. 3D isosurfaces of the ambient coronal density, n, viewed from a number of different vantage points. These vantage points, defined by $\theta_{\rm axis}$ and $\varphi_{\rm axis}$, are in or near the ecliptic plane for panels (a)–(c), at northern latitudes for panels (d)–(f), and at southern latitudes for panels (g)–(i). The green circle in each panel corresponds to a heliocentric distance of 10 $R_\odot$ in the ecliptic.

fixed Sun-centered radial ($\theta_{\rm s/c} = 0°$ and $\varphi_{\rm s/c} = -125°$). The inner edges of each FOV in Figures 3(b)–(d) is adaptively occulted to be at a fixed radial distance of 2 $R_\odot$ in the POS, and the corresponding outer edge is fixed to be at 90° elongation. Supposing that such a notional imager moves toward the Sun, (1) its FOV coverage in terms of radial distance will become smaller, (2) the WL brightness that it images I will become more intense, while the dynamic range of I will be reduced, (3) the brightness patterns of coronal streamers will remain almost unchanged, and (4) radial gradients in normalized brightness, Norm.(I), will remain sharp (Figures 3(b)–(d)). The virtually

unchanged brightness patterns of coronal streamers shown in Figures 3(b)–(d) are ascribed to the cocoon-like isosurface of coronal density seen in Figure 2. The brightness patterns of coronal emission, weakly dependent on viewing distance $r_{\rm s/c}$, are chiefly determined by viewing perspective, i.e., latitude $\theta_{\rm s/c}$ and longitude $\varphi_{\rm s/c}$. The degree of polarization, p, of coronal emission is abruptly enhanced from 0.4 for elongation $\varepsilon \leqslant 40°$ to 0.9 near $\varepsilon = 90°$ (Figures 4(b)–(d)). A stream of global polarized images in broadband WL would be a powerful asset for localizing 3D features in the corona and heliosphere, as demonstrated by the concept study for the *PUNCH*
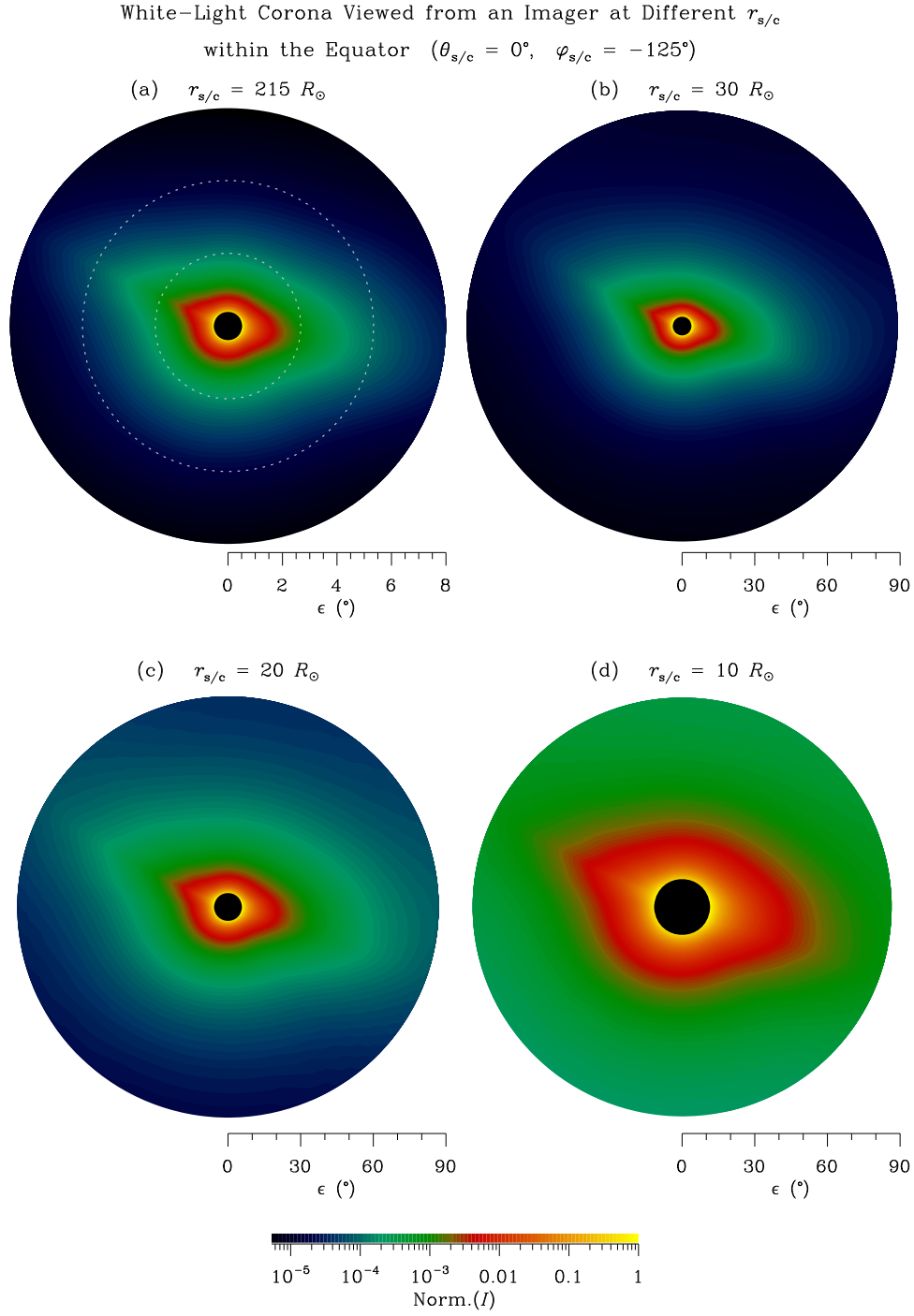
Figure 3. WL brightness, I, of the corona as imaged from different viewpoints at $r_{s/c} = [215, 30, 20, 10] R_\odot$ from Sun center along a fixed radial (defined by $\theta_{s/c} = 0°$ and $\varphi_{s/c} = -125°$). The FOV extends to an elongation ε of 8° in panel (a) and 90° in panels (b)–(d). Concentric dotted circles in panel (a) correspond to heliocentric distances of 20 and 10 $R_\odot$ in the POS.

(Polarimeter to UNify the Corona and Heliosphere) SMall-EXplorer (SMEX) mission, selected for study by NASA in 2017. The dependence of the Thomson-scattering emission from the corona on imaging geometry (Jackson et al. 2010; Xiong et al. 2013a) dictates that (1) WL brightness I at elongation $\varepsilon \approx 90°$ is contributed by plasma in the locality of the imager, and (2) I at $\varepsilon \approx 40°$ is contributed by plasma over a broad range of scattering angles centered on the Thomson sphere. The "inner" and "outer" FOVs, which we define as being within and beyond $\varepsilon \approx 40°$, respectively, become

effectively an "in situ subimager" and a "remote-sensing subimager." Hence, the signal collected within the full wide-field FOV originates from a combination of WL emission from both remote and local plasmas. Such WL "in situ imaging" was first reported in the analysis of the 90° photometer on *Helios*, which detected an increase in brightness whenever a CME crossed the spacecraft (Jackson & Leinert 1985). Viewing along an elongation angle of $\varepsilon \approx 90°$, *PSP*/WISPR will serve as an "in situ imager," being very sensitive to emission from plasma close to the spacecraft.

White–Light Corona Viewed from an Imager at Different $r_{s/c}$

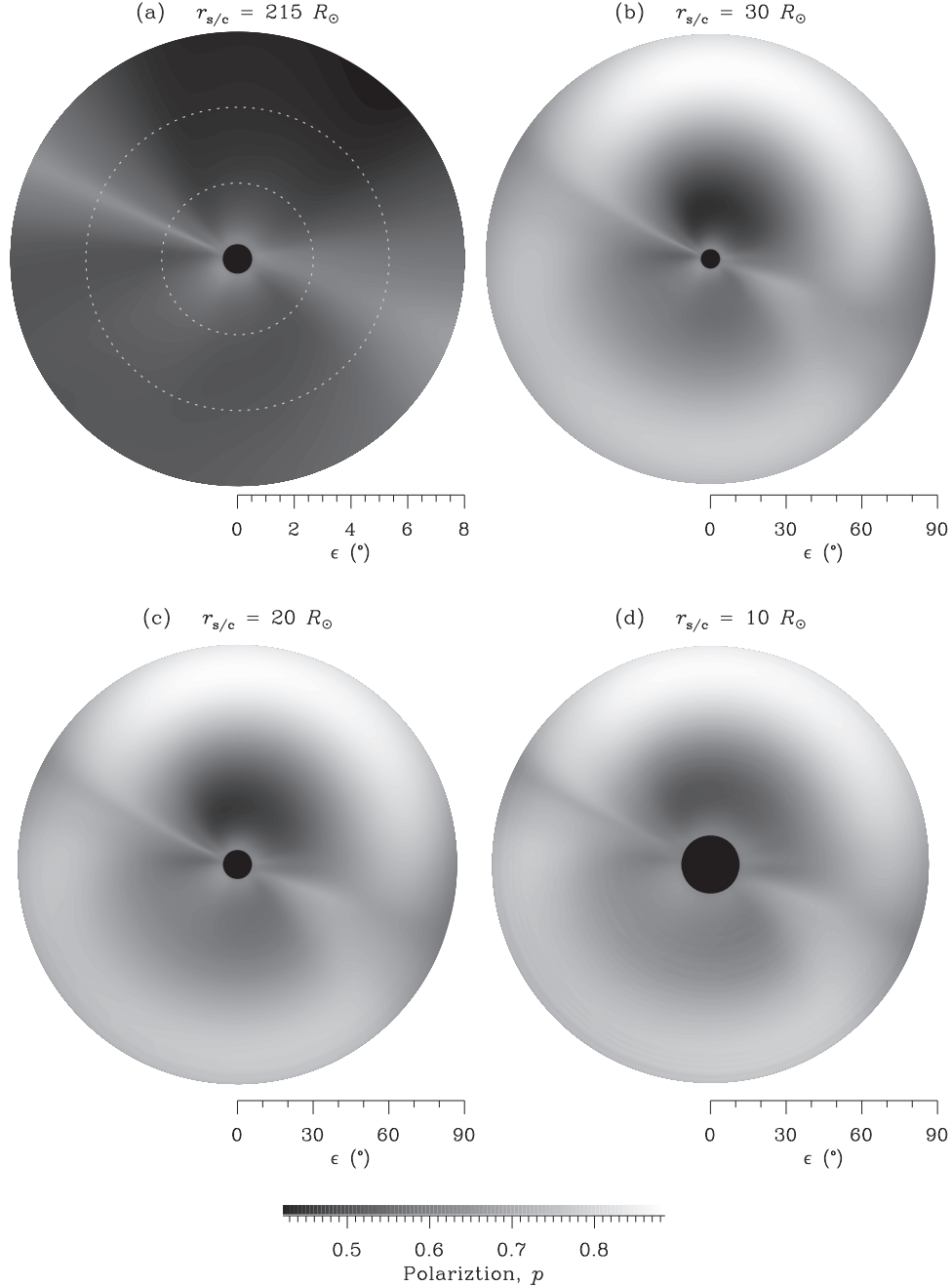within the Equator $(\theta_{s/c} = 0°, \quad \varphi_{s/c} = -125°)$

(a) $r_{s/c} = 215\ R_\odot$ (b) $r_{s/c} = 30\ R_\odot$

0   2   4   6   8   0   30   60   90
ϵ (°) ϵ (°)

(c) $r_{s/c} = 20\ R_\odot$ (d) $r_{s/c} = 10\ R_\odot$

0   30   60   90   0   30   60   90
ϵ (°) ϵ (°)

0.5   0.6   0.7   0.8
Polariztion, p

Figure 4. Same as Figure 3, but for the degree of polarization p.

PSP/WISPR will be able to provide the large-scale context for the solar wind structures later encountered by the in situ particle and field instruments. Prior to each *PSP* perihelion, WISPR will act as an "in situ imager" along viewing elongations $\varepsilon \approx 90°$. Then, synoptic coronal images taken by WISPR can be used to predict when *PSP* will cross a solar wind structure of interest (e.g., a heliospheric plasma sheet boundary, a heliospheric current sheet surface, or a CIR interface). Such coordination of observations from WISPR and the in situ instruments (i.e., FIELDS, SWEAP, and ISIS-EPI) is crucial in addressing the scientific objectives of the *PSP* mission. The dependence of WL emission at an elongation

$\varepsilon \approx 90°$ with the longitude φ of the viewing platform is shown in Figure 5. This "in situ imager" on board its notional host spacecraft is traveling in a circular orbit within the equator. All LOSs viewed from the spacecraft at $\varepsilon = 90°$ define a plane perpendicular to the Sun–spacecraft line. Among these 90°-elongation LOSs are two that lie within the ecliptic, east and west of the spacecraft. A spacecraft that is west (or east) of a CIR would receive the eastern (or western) emission from that CIR. The maximum WL radiance from the east of a CIR is generally larger than that from the west, as eastern LOSs viewed from a WL imager located west of the CIR are better aligned with the spiral-like density ridge of the CIR. The
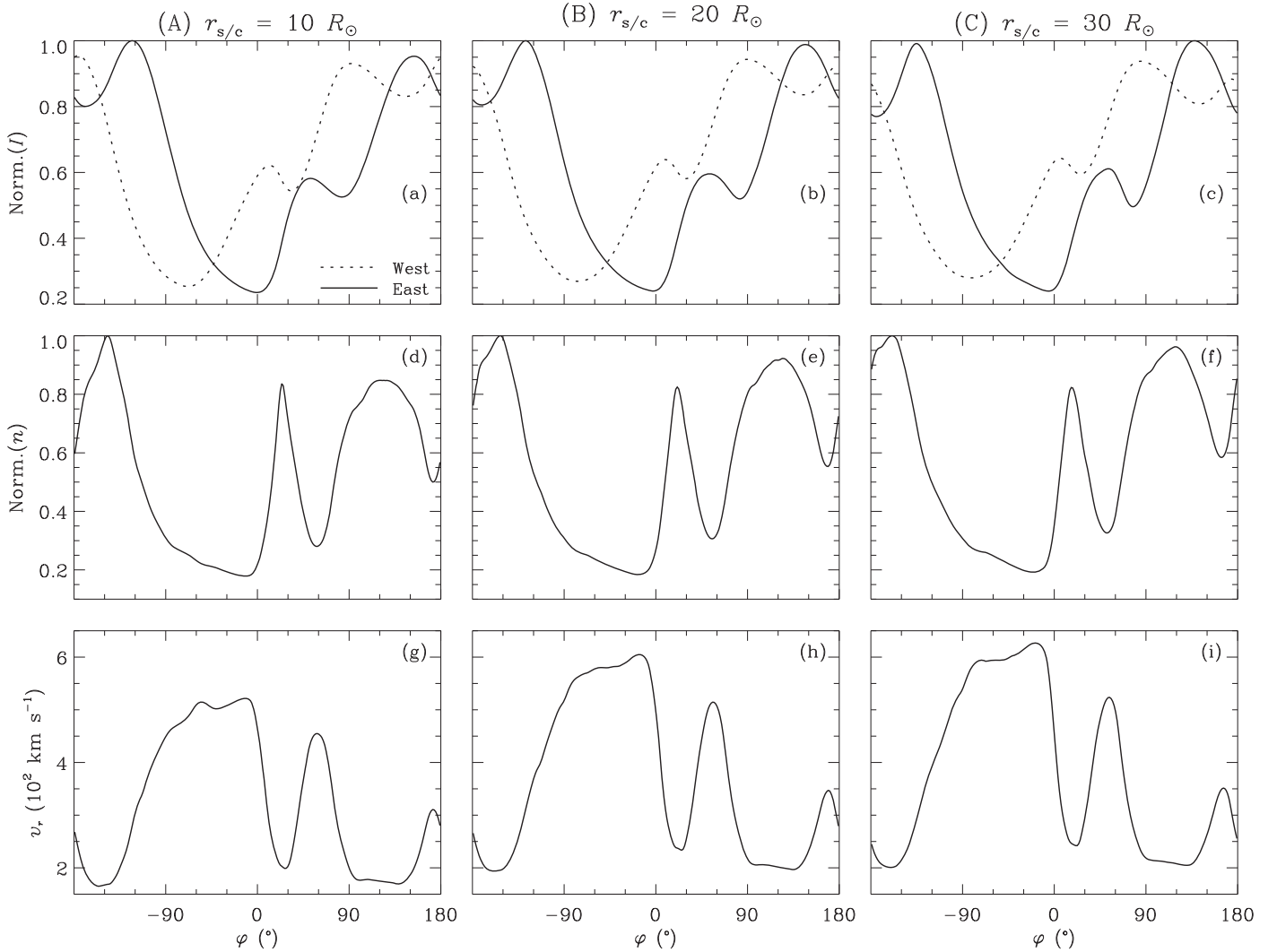
Figure 5. Longitudinal dependence of normalized WL brightness I (panels (a)–(c)), proton density n (panels (d)–(f)), and radial speed v_r (panels (g)–(i)) observed by a notional spacecraft in heliocentric circular orbit in the ecliptic plane. The solid and dashed lines in panels (a)–(c), respectively, denote the eastern and western emission along elongation $\varepsilon = 90°$. The heliocentric distance $r_{s/c}$ of the ecliptic spacecraft is $10\,R_\odot$ for column (A), $20\,R_\odot$ for column (B), and $30\,R_\odot$ for column (C).

eastern and western WL brightness, I, are depicted as solid and dashed lines, respectively, in Figures 5(a)–(c). Both exhibit a similar trend with respect to longitude, φ. The longitudinal variation of I is caused by the nonuniformity in the density, n, along the spacecraft orbit. In the $I − \varphi$ curves shown in Figures 5(d)–(f), the maximum density is almost five times the minimum density. Correspondingly, the difference between the maximum and minimum brightness is also around five-fold (Figures 5(a)–(c)), for both eastern and western emission. Three coexisting CIRs can be identified from the anticorrelation between the density, n, and speed, v_r, of the solar wind streams (Figures 5(d)–(i)). For example, three local density peaks at longitudes of $−150°$, $30°$, and $120°$ shown in Figure 5(d) indicate the positions of the CIRs in the equatorial plane at a distance $r_{s/c} = 10\,R_\odot$ from the Sun. Within close proximity to the CIR at $r_{s/c} = 10\,R_\odot$ and $\varphi = 120°$ are peaks in the eastern radiance (at $\varphi = 150°$) and the western radiance (at $\varphi = 90°$). The longitudinal difference of $30°$ between the location of the observing spacecraft and that of the observed CIRs corresponds to the time delay between a CIR's radiance signature and its

in situ particle/field signature. This short time delay between coordinated WL-imaging and in situ observations of CIRs can be accurately estimated on the basis of the longitudinal distribution of observed CIRs and the orbital speed of the observing spacecraft.

4. WL Imaging and In Situ Measurements of CIRs from the In-ecliptic *PSP*

As one of the most ambitious missions to date, *PSP* is expected to be the first man-made object to enter a star's corona. *PSP*, which remains close to the ecliptic, will use repeated gravity assists from Venus to incrementally decrease its orbital perihelion, eventually performing multiple passes within $10\,R_\odot$ of the Sun. *PSP* will undertake 24 near-Sun passes (<0.2 au) during the nominal mission duration of 6.9 years. Its final orbital configuration is characterized by a perihelion $9.86\,R_\odot$, an aphelion 0.73 au, an inclination of $3°.4$ from the ecliptic, and an orbital period of 88 days. Here, we assign any time within the 88 day orbit of *PSP* as having a value between $−44$ and 44 days, where 0 corresponds to

Trajectory of *Parker Solar Probe*
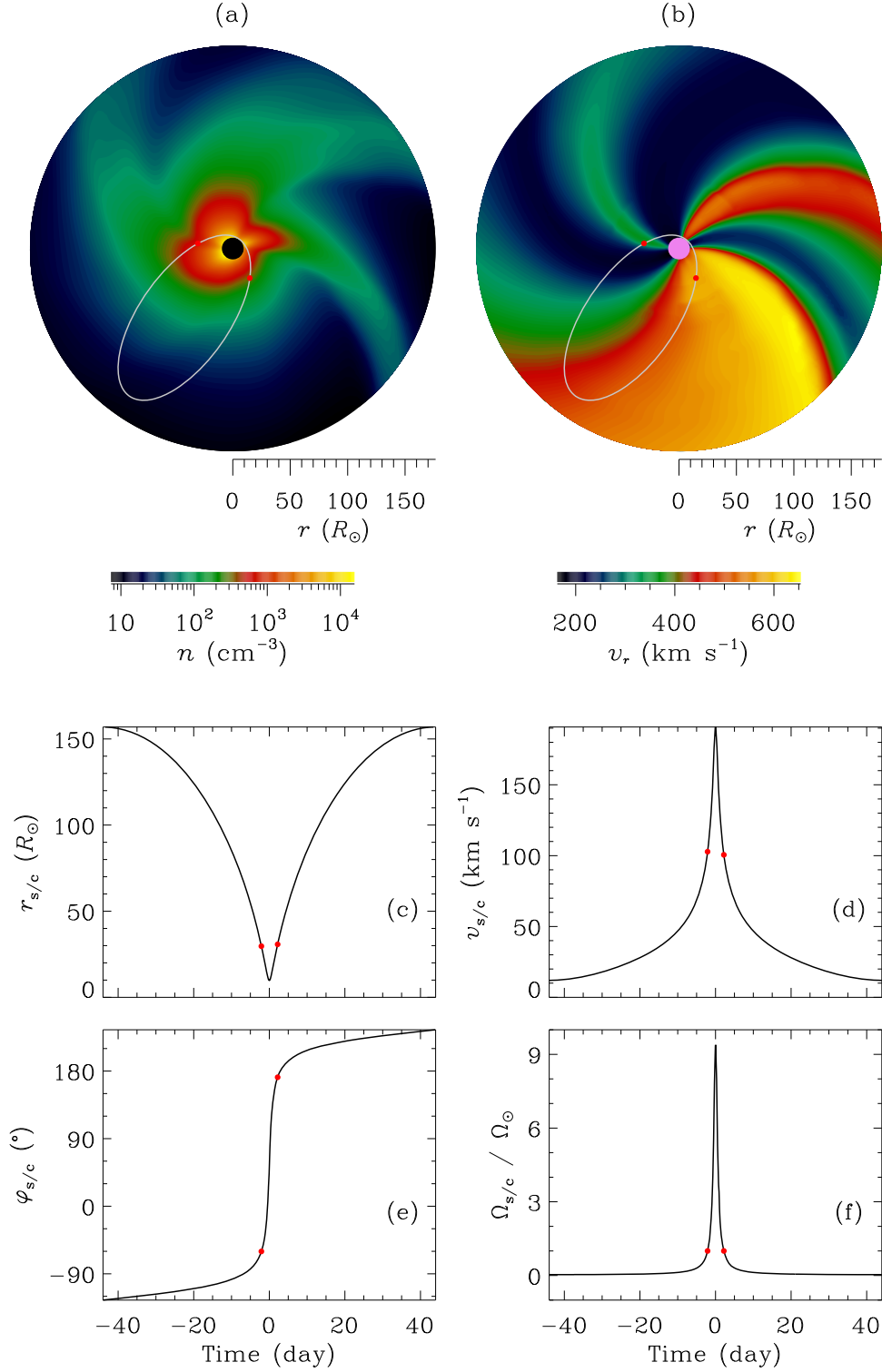## in a Static Coordinate System

Figure 6. The ultimate orbit of *PSP* in a static coordinate system, superimposed on the background distribution of solar wind density, n (panel (a)), and speed, v_r (panel (b)), within the *PSP* orbital plane. The *PSP* oribt is plotted in terms of its radial distance, $r_{s/c}$ (panel (c)), orbital speed, $v_{s/c}$ (panel (d)), longitudinal position, $\varphi_{s/c}$ (panel (e)), and Sun-centered angular speed, $\Omega_{s/c}$ (panel (f)), as a function of orbital cruise time in days (from aphelion). The red dots marked on panels (a)–(f) indicate the occasions when *PSP* exactly corotates with the Sun, i.e., when $\Omega_{s/c} = \Omega_\odot$ (panel (f)).

perihelion. The final orbit of *PSP* is marked with solid white ellipses in Figures 6(a)–(b), overlaid on isocontours of solar wind density n (Figure 6(a)) and radial speed v_r (Figure 6(b)) within *PSP*'s orbital plane. As *PSP* travels from perihelion to aphelion, its orbital linear speed $v_{s/c}$ increases from 10 to 190 km s^{-1} (Figure 6(d)). Given a solar rotation period of
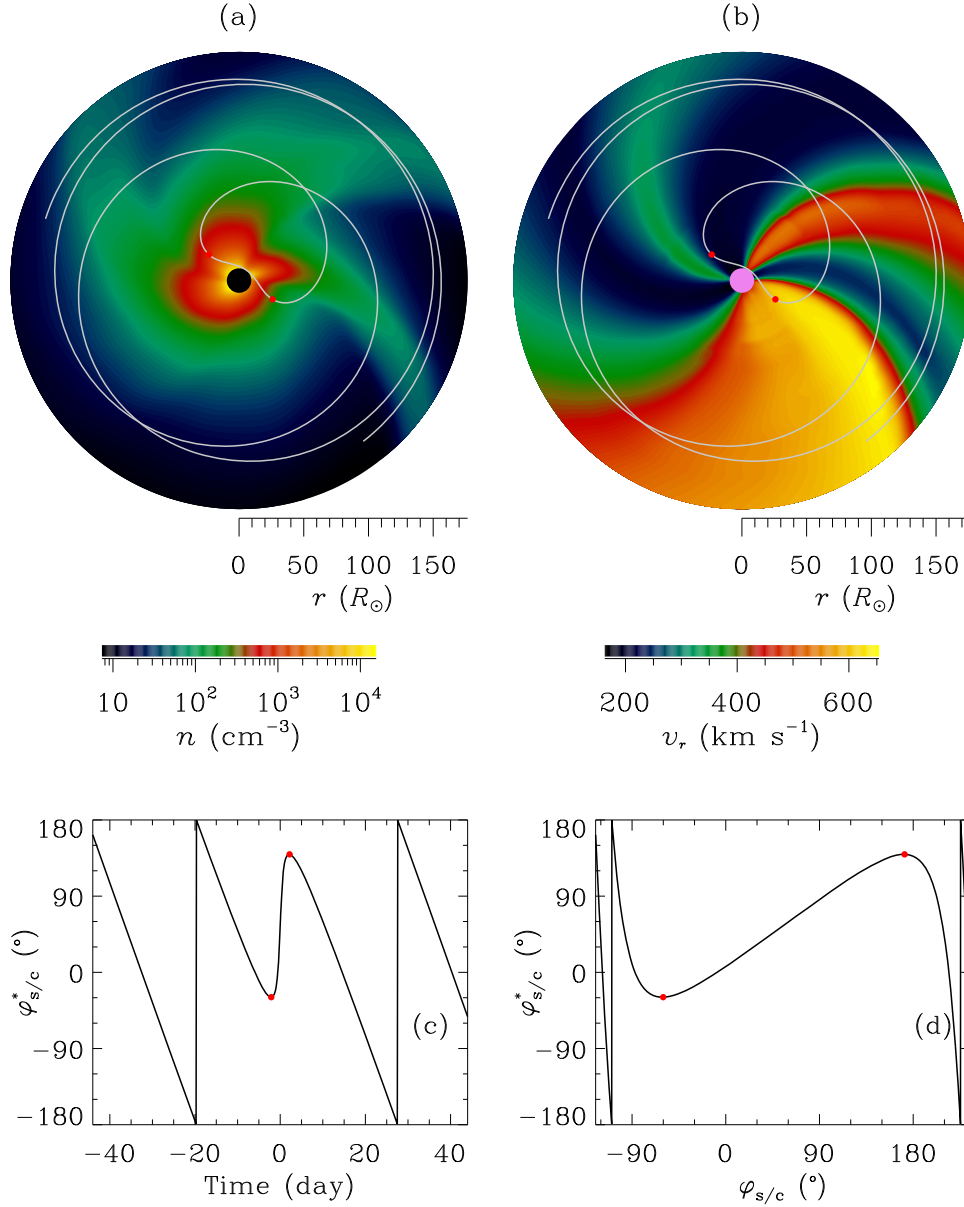
Figure 7. Same as Figure 6 but for the *PSP* orbit ($r_{s/c}$ and $\varphi^*_{s/c}$) depicted in a corotating coordinate system. As shown in panel (d), the longitude in a corotating system is plotted as a function of that in a static frame.

27 days at the equator, the ratio between *PSP*'s orbital angular speed and solar rotation $\Omega_{s/c}/\Omega_\odot$ increases markedly to 9.5 at perihelion (Figure 6(f)). $\Omega_{s/c}$ varies much faster with time than $v_{s/c}$. The times when *PSP* exactly corotates with the Sun ($\Omega_{s/c} = \Omega_\odot$) are marked as two red dots in Figure 6. At these times, the heliocentric distance of *PSP* is around $30\,R_\odot$ (Figure 6(c)). The outer boundary of the outer corona is traditionally taken to be at $30\,R_\odot$, corresponding to the outer edge of the FOV of Lasco/C3 on board *SOHO*. *PSP* enters the outer corona at a relatively high speed of $100\,\mathrm{km\,s^{-1}}$, spending around 4.22 days within the corona (from longitude $-80°$ to $180°$) before emerging from there (Figure 6(e)). The spacecraft spends 11.26, 8.62, 6.16, 4.22, 2.29, and 0.35 days, respectively, within 60, 50, 40, 30, 20, and $10\,R_\odot$. *PSP* sequentially crosses

nearly all of the simulated background solar wind streams and CIRs within its orbital plane. To reconstruct the quiescent large-scale solar-wind streams that *PSP* will encounter, both solar rotation and spacecraft trajectory need to be considered. The Sun-centered angular speed of *PSP* increases from aphelion at 0.73 au to perihelion at $9.86\,R_\odot$, with the spacecraft rotating faster than the Sun inside about $30\,R_\odot$. When transformed from a static into a corotating coordinate system, an elliptical *PSP* orbit (Figure 6) becomes a multiwinding spiral (Figure 7). The winding number around the Sun varies between 2 and 3 over one full *PSP* orbit, as seen from the longitudinal position $\varphi^*_{s/c}$ with the modification of solar rotation (Figure 7(c)). Transition of $\varphi^*_{s/c}$ between $-180°$ and $180°$ in Figures 7(c)–(d) arise due to

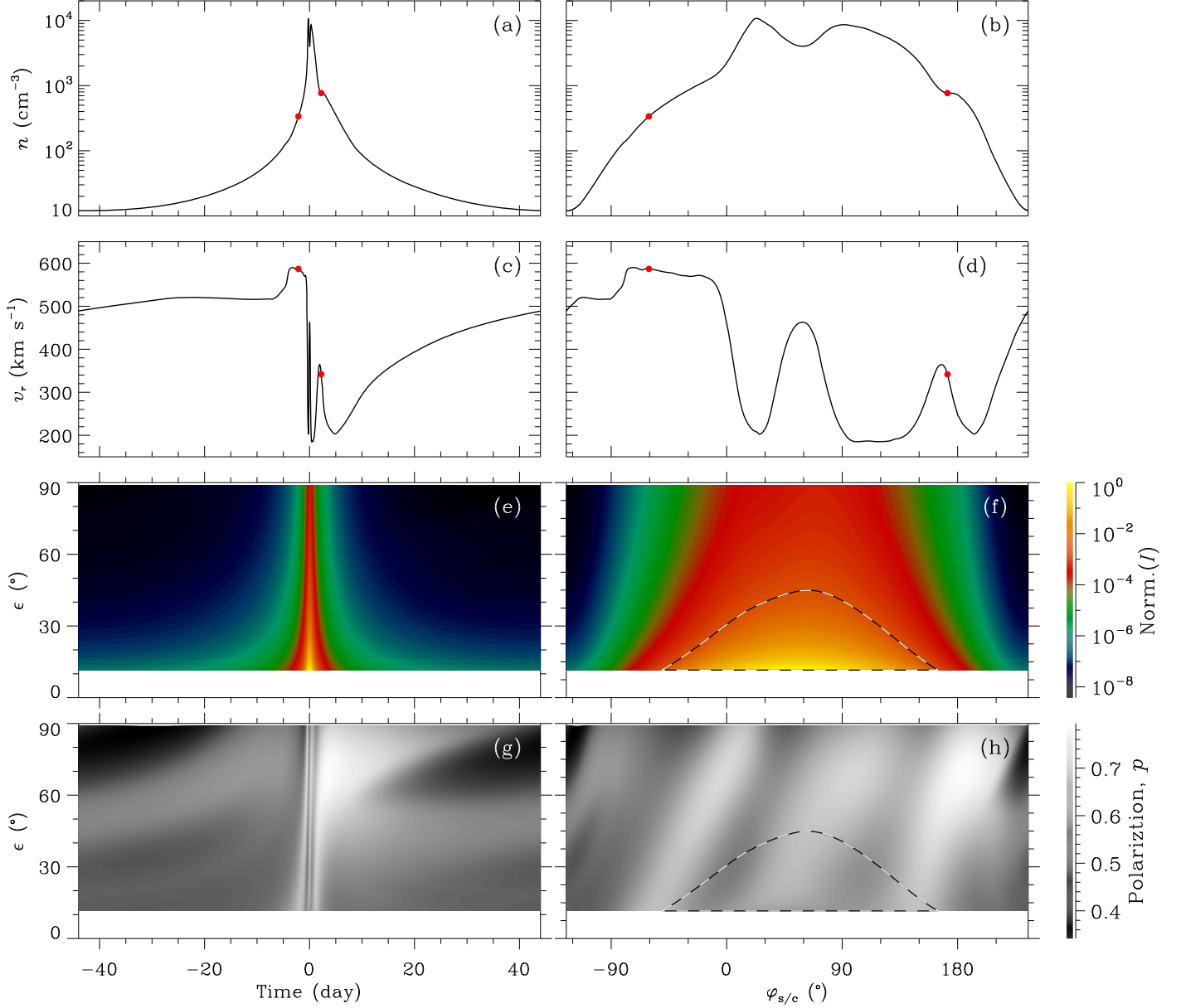## In−Situ and Remote−Sensing Observations in a Static Coordinate System

Figure 8. In situ and remote-sensing observations of the ambient solar wind flows along the *PSP* orbit, as depicted in a static coordinate system (as in Figure 6). The observed solar wind density n, speed v_r, WL radiance I, and degree of polarization p are presented, from top to bottom, as a function of *PSP*'s cruise time (left-hand column) and longitudinal position (right-hand column). The red dots in panels (a)–(d) correspond to the occasions when *PSP* corotates with the Sun. The black–white dashed lines in panels (f) and (h) enclose a region where radiance exceeds the threshold Norm.(I) ⩾ 0.0035.

aliasing, as values of $\varphi_{s/c}^* = \pm 180°$ correspond to the same position in the *PSP*'s orbital plane. Ignoring the aliasing, the sign of $\varphi_{s/c}^* - \varphi_{s/c}$ curve reverses only on the two occasions when $\Omega_{s/c} = \Omega_{\odot}$ (Figure 7(d)). As *PSP* exactly corotates with the Sun twice per orbit, the innermost winding of its orbit when transformed into the corotating framework adopts the form of a closed "heart shape" inside around $80\,R_{\odot}$. *PSP*, traveling along the "heart shape" trajectory, can cross a single CIR twice. This enables *PSP* to make in situ measurements of the same CIR in both the corona and heliosphere.

Synthesized *PSP* in situ and remote-sensing observations of ambient solar wind flows are shown, with and without solar rotation respectively, in Figures 8 and 9, respectively. The effect of solar rotation is negligible, as seen during *PSP*'s flyby

from $\varphi_{s/c} = -60°$ to 180°. A CIR can be identified in in situ measurements via its characteristic anticorrelation between density n and speed v_r, while the same CIR is manifest in WL imagery as an antisunward moving brightness front. Due to solar rotation, each of the three equatorial CIRs simulated in this paper is repeatedly crossed by *PSP* during a single orbit (Figures 7(a)–(b)). The synthesized *PSP* signatures of CIRs, shown in Figure 9, are determined by the ambient solar wind distribution and the spacecraft trajectory. As *PSP* approaches perihelion, the WL radiance from the corona, at small elongations, increases in intensity (Figure 9(f)). Polarization measurements, which manifest as inclined black and white tracks in Figure 9(h), can be used to localize the main scattering region that is the source of the received WL emission

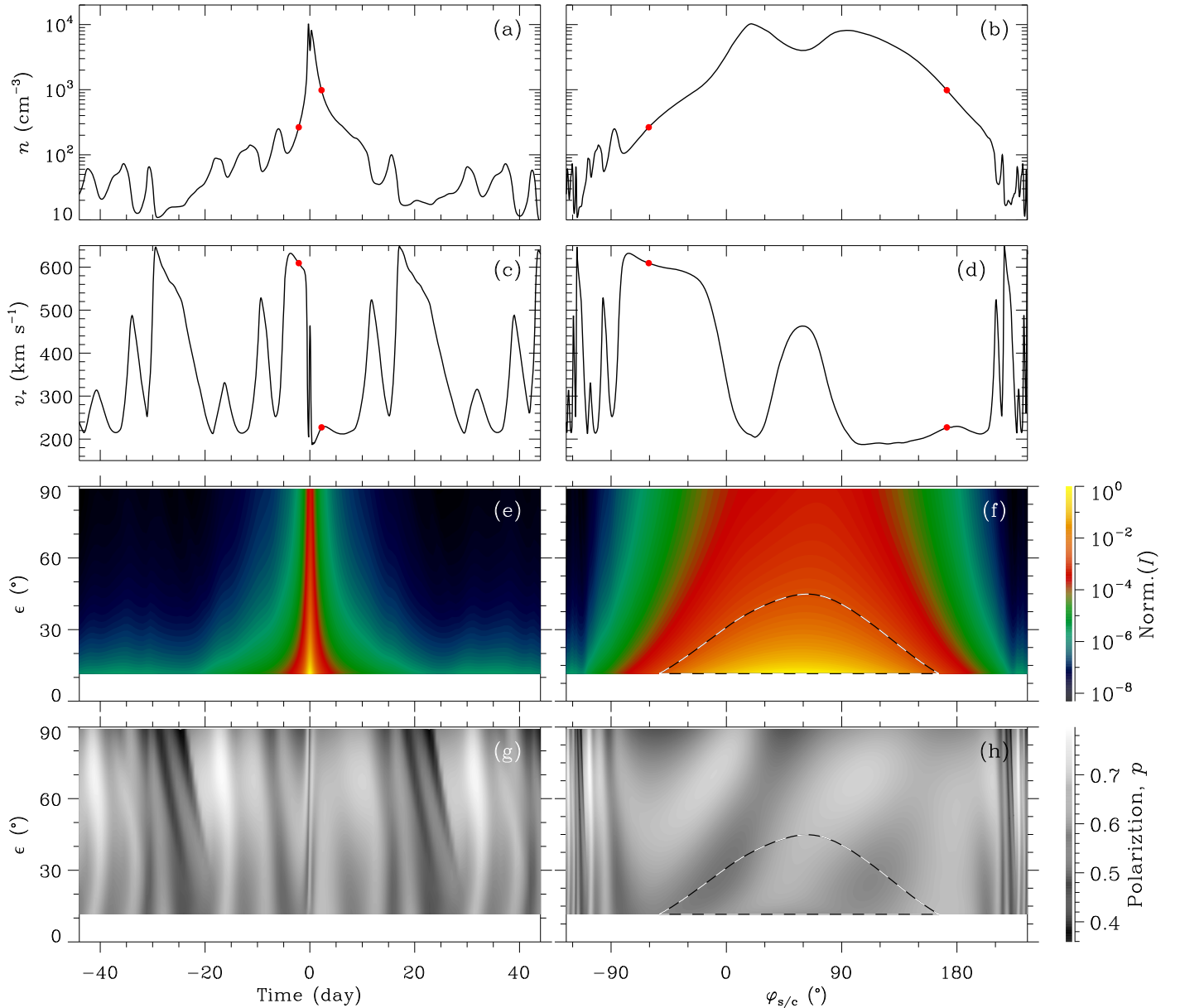In-Situ and Remote-Sensing Observations in a Co-rotating Coordinate System

Figure 9. Same as Figure 8 but for the *PSP* orbit depicted in a corotating coordinate system (as in Figure 7).

(Xiong et al. 2013a, 2013b). This main scattering region, in a static coordinate system, is enclosed by the black–white dashed line in Figure 10. For the more realistic situation in which solar rotation is considered (i.e., in a corotating system), the main scattering region is smaller (Figure 11). The brightness patterns that are observed during a fast *PSP* flyby of the Sun (Figures 9(f), (h)) are caused by the coronal and heliospheric plasmas inside the main scattering region (Figure 11). Within this region at *PSP* perihelion, the plasma density distribution is relatively homogeneous, the solar wind flow speed distribution is highly heterogeneous, and there are multiple physical processes that drive that solar wind flow. These processes include (1) a fast solar wind flow rapidly accelerated from 0 to $400\,\mathrm{km\,s^{-1}}$, (2) a slow solar wind flow no higher than $150\,\mathrm{km\,s^{-1}}$, and (3) an interface between the fast and slow flows that is the source of CIR formation.

There is still controversy over how CIRs develop and change their latitudinal/longitudinal transition layers from the corona into the heliosphere. Schwenn et al. (1978) found, from *Helios* observations, that the latitudinal/longitudinal edges of the high-speed solar wind streams from coronal holes are very sharp, with gradients of $100\,\mathrm{km\,s^{-1}}\,\mathrm{deg^{-1}}$ near 0.3 au. Such sharp edges are less apparent in the *Ulysses* and near-Earth data, perhaps due to the evolving profile of the leading edges of CIRs and interplanetary dispersion on the trailing edges. However, the Wang & Sheeley (1990) numerical model of the solar corona, which relates the expansion of magnetic flux tubes to the speed of the solar wind by assuming that slow solar wind originates at the boundaries of coronal holes, suggests that the latitudinal/longitudinal edges of streams near the Sun are broad regions with gradients of only $20\,\mathrm{km\,s^{-1}}\,\mathrm{deg^{-1}}$. The nature of CIR transition layers is expected to be clarified by the *PSP* observations. If a CIR survives for one or
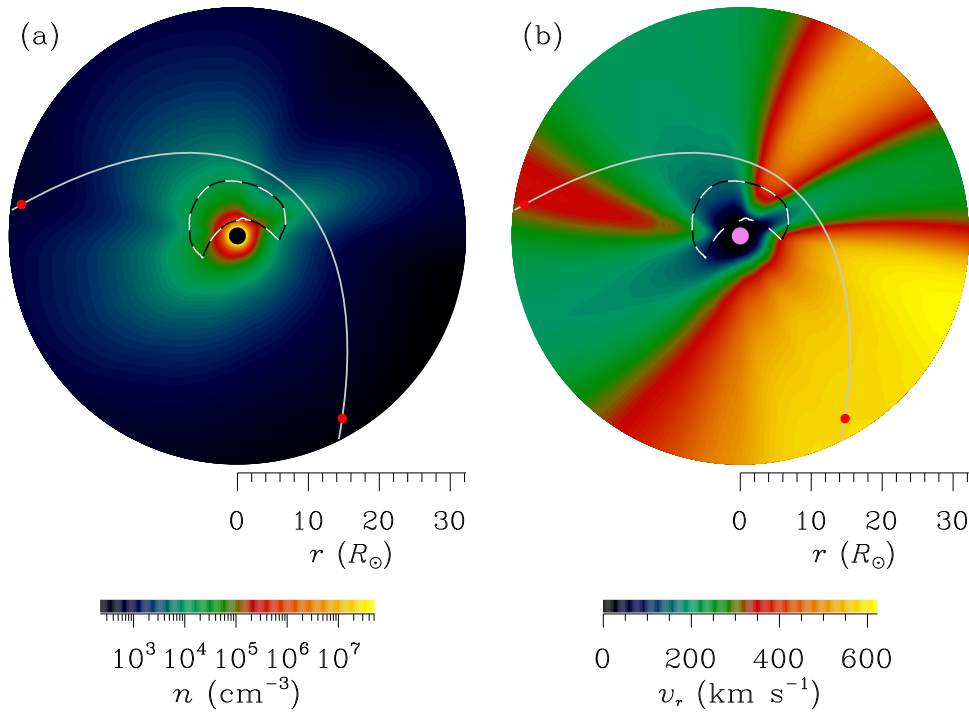
Figure 10. The main scattering region of the received WL radiance *I* along the *PSP* orbit, depicted in a static coordinate system (as in Figure 6). The near-Sun location of the main scattering region (enclosed in a black–white dashed line) is inferred from the polarized brightness measurements (as shown in Figures 8(f) and (h)).
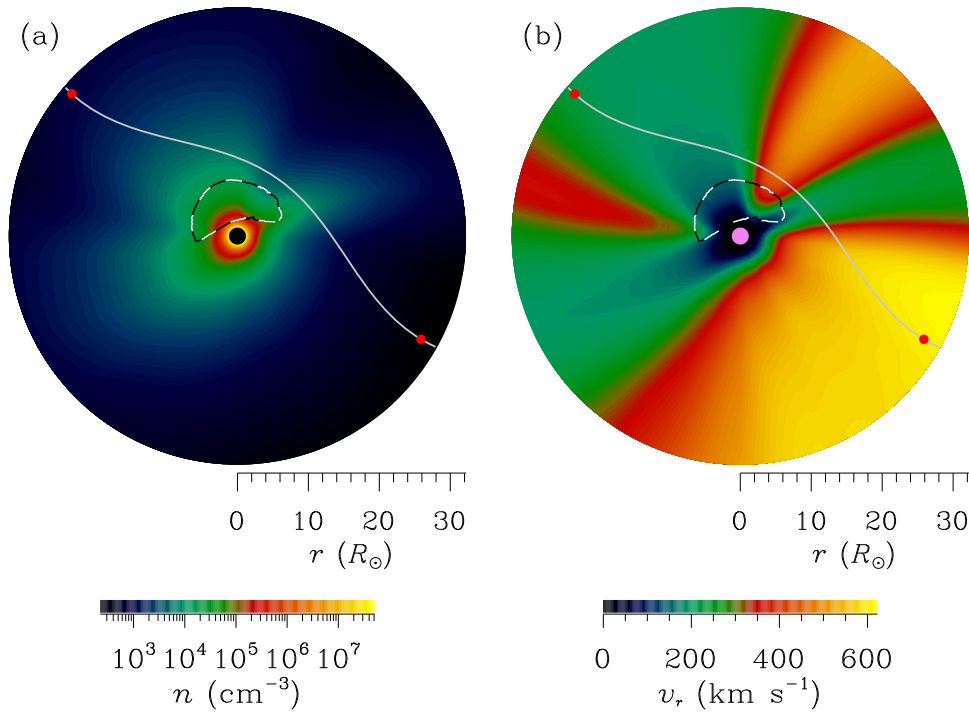

Figure 11. The main scattering region of the received WL radiance *I* along the *PSP* orbit, depicted in a corotating coordinate system (as in Figure 7).

more solar rotations, *PSP* can cross that CIR multiple times during a single orbit. As each crossing of the CIR is at a different heliocentric distance, longitudinal transition layers detected during multiple *PSP* crossings can be compared in order to assess CIR development. With remote-imaging and in situ instruments on board *PSP*, one CIR can be continuously traced from its source in the corona to maturity in the heliosphere.

5. WL Imaging of CIRs from the Out-of-ecliptic *SolO*

The WL imager (WISPR) on board the in-ecliptic *PSP* spacecraft integrates any longitudinal information about the solar wind plasma distribution. However, additional polarization measurements of brightness patterns in WL images can be used to infer the spatial positions of solar wind flows, as demonstrated in Figure 11. In situ instruments on board *PSP* can sample solar wind streams shortly after they can be detected in WL, as these structures ascend from the Sun toward the spacecraft. The short time delay between the first detection of a solar wind feature in WL imagery and measurement of its in situ signature, when *PSP* is near the perihelion, can be exploited to infer the longitudinal distribution of solar wind structures, as shown in Section 3. More direct information on longitudinal structures near the ecliptic plane can be provided by observations from *SolO*-HI, from an OOE perspective. The 3D density distributions of the quiescent CIRs studied in this paper, from various perspectives, are presented in Figure 12. Because of the solar minimum conditions under which they are simulated, both the 3D CIRs in Figure 12 and the 2D coronal streamer belt in Figure 1 are constrained to low and intermediate latitudes. The WL emission from these CIRs is synthesized as WL brightness images in Figure 13. An OOE WL imager can be used to resolve the spiral morphology of CIRs, to differentiate multiple coexisting CIRs, and to track each heliospheric CIR back toward its coronal source (Xiong et al. 2017). Moreover, the background CIRs and transient CMEs can be readily differentiated from an OOE WL perspective, because the WL radiance patterns of CIRs and CMEs observed by an OOE WL imager are characterized as spirals and arcs, respectively (Xiong et al. 2018).

The heliocentric distance of the *STEREO* orbit is roughly 1 au, whereas that of the *SolO* orbit is ultimately reduced to $60\,R_\odot$ after multiple Venus gravity assists. Unprecedented close-up WL imaging of solar wind streams within the orbit of Venus will be achieved by the forthcoming *SolO* spacecraft, from $60\,R_\odot$, and by *PSP*, from less than $10\,R_\odot$. In contrast to WL imaging enabled by *STEREO*/HI at 1 au, *SolO*-HI from $60\,R_\odot$ will be able to detect much more intense WL emission from CIRs, with much higher spatial resolution. The WISPR instrument on board *PSP* is capable of resolving the fine substructures of CIR sources near the Sun, while SolO-HI will be able to map the large-scale morphology of heliospheric CIR. A single CIR, from corona to heliosphere, can be jointly observed via (1) in situ measurements from *PSP*'s particle/field instruments, (2) close-up edge-on imaging from the side by *PSP*/WISPR, (3) OOE imaging from the top or bottom by *SolO*-HI, and (4) possibly via in situ measurements from the *Bepi-colombo* orbiting the Mercury and other spacecraft near 1 au. The potential of ambitious synergies between these highly complementary deep-space missions (i.e., *PSP*, *SolO*, *Bepi-colombo*, etc.) will constitute a significant milestone in exploring the corona and heliosphere in 3D.

6. Discussion and Summary

Imaging the corona and heliosphere via Thomson-scattered photospheric light has proved crucial to understand the background solar wind and transients therein. WL radiance decreases rapidly with increasing elongation, from the corona to the heliosphere. Such WL radiance is not only contributed by Thomson scattering from interplanetary electrons and dust. The F-corona, zodiacal light, star field, and residual solar stray light all obscure the faint Thomson-scattered signals from CMEs and coronal streamers, and constitute the main background sources for any deep-space WL imager. Although bright, these background signals are, fortuitously, relatively stable (Leinert & Pitz 1989). In particular, the very stable emission from the F-corona and zodiacal light can be accurately subtracted from the *SOHO*/LASCO/C3 and *STEREO*/SECCHI/HI images, because these spacecraft of *SOHO* and *STEREO* are at a more-or-less fixed distance from the Sun. Even more accurate and robust photometry analyses will be needed to separate the F-corona and zodiacal light from the Thomson-scattered light imaged by the *PSP*/WISPR and *Solo*-HI instruments, due to the rapidly evolving nature of the *PSP* and *SolO* orbits. As the WL brightness from corona to heliosphere covers a very high dynamic range, a single WL imager is limited in terms of the elongation coverage of its FOV, and a suite of WL imagers such as *STEREO*/SECCHI is required to cover the full corona–heliosphere elongation range. The specifications of a WL imager (such as photometric sensitivity, cadence, and FOV coverage) must be carefully optimized according to the observational requirements necessitated by the mission science objectives and the engineering constraints of interplanetary orbit. The ecliptic elongation coverage of *STEREO*/HI is approximately $4°$–$88°.7$; for *PSP*/WISPR, it is $13°.5$–$108°$. Like *STEREO*/HI, *PSP*/WISPR comprises two wide-field telescopes, each of which has a relatively small aperture size. As the heliocentric distance of *PSP* rapidly changes, WISPR needs to acquire rapid sequences of images with highly variable signal content across the large FOV.

The 2D brightness patterns of Thomson-scattered WL in the corona and heliosphere depend significantly on 3D viewing angle. As a high-density interplanetary plasma structure, such as a background CIR or transient CME, occupies a significant 3D volume, different parts of the structure will contribute most significantly to the radiance pattern captured by WL imagers situated at different heliocentric longitudes and latitudes (Xiong et al. 2013a). To date, the corona and heliosphere have only ever been imaged in WL from an in-ecliptic perspective, hence longitudinal dimension has been integrated. The only OOE spacecraft, *Ulysses*, hosted no imaging instruments. WL imagers are recognized as having a crucial role in realizing the scientific objectives of OOE space observatories such as the upcoming *SolO* mission and other mission concepts such as *SPI*, *POLARIS*, *SPORT*, and *InterHelioProbe*. Lessons in how to optimize a prospective solar polar orbiting mission should be learned from *SolO* and *Ulysses* missions, and also from *STEREO* and *SOHO*. An OOE WL imager in a solar polar orbit would permit the mapping of near-ecliptic large-scale density structures (Xiong et al. 2017, 2018).

The complex Sun-heliosphere system, and the space weather transients that propagate within, are currently being observed by a fleet of deep-space spacecraft carrying remote-sensing
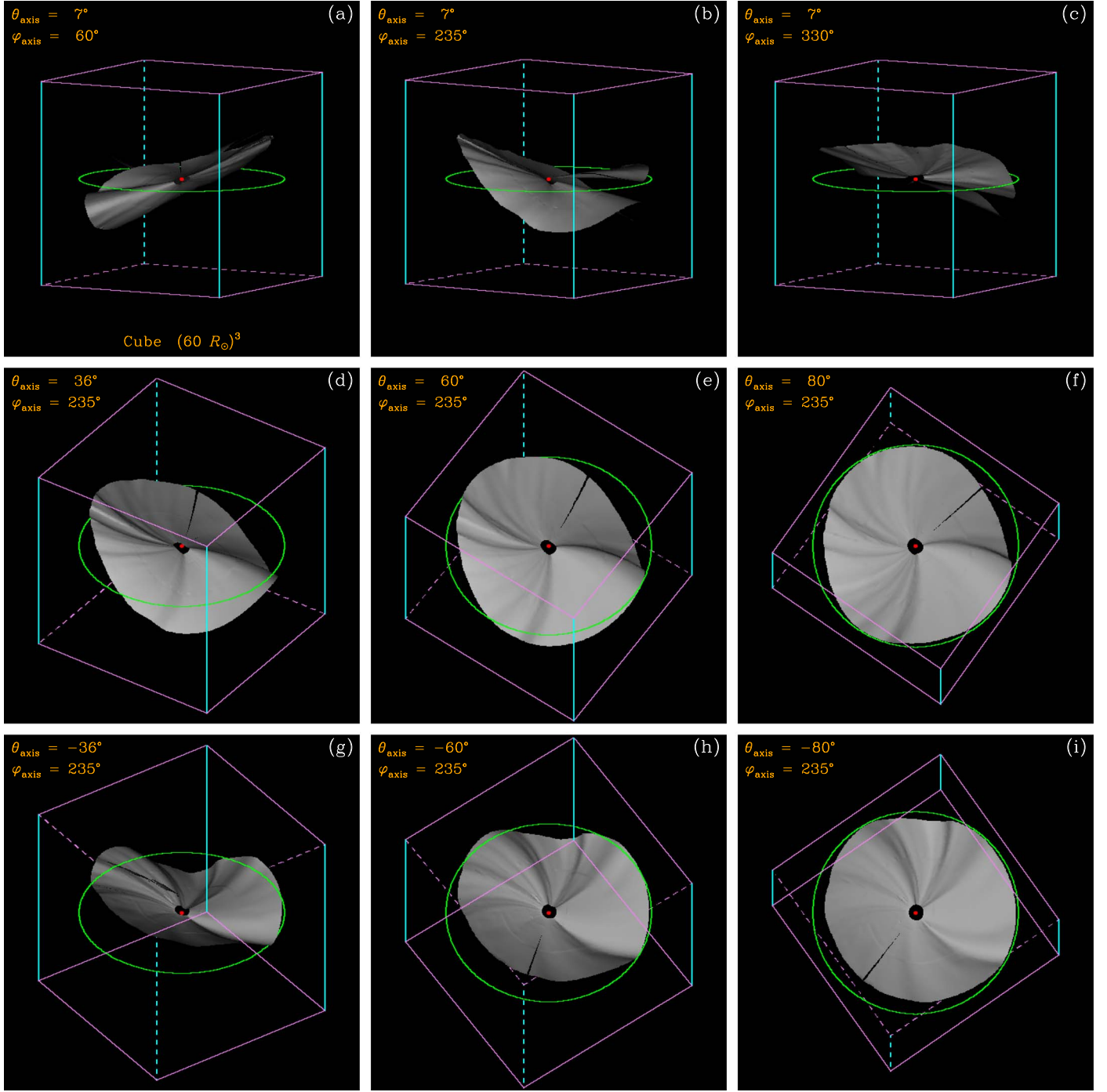
Figure 12. 3D isosurfaces of the normalized solar wind density, $n\,r^2$, inside a heliocentric distance of 60 $R_\odot$, as viewed from a number of different vantage points defined by $r_{\mathrm{axis}} = 60\,R_\odot$, $\theta_{\mathrm{axis}} = [7°, \pm36°, \pm60°, \pm80°]$ and $\varphi_{\mathrm{axis}} = [60°, 235°, 330°]$.

instrumentation observing at WL, EUV, and X-ray wavelengths, as well as in situ instruments making measurements of interplanetary particles and fields. The orbit and scientific payload of a deep-space spacecraft mission should be carefully optimized to maximize the scientific return within the limitation of spacecraft engineering resources (e.g., mass, power, memory, and telemetry rate). Indeed, the orbit and WL imaging payload of such a spacecraft should be considered holistically, through the conception, design, and manufacturing phases of a deep-space mission. WL imaging of the corona and heliosphere from deep space is mature in terms of its technology readiness level, given many years of successful operation of the two

coronagraphs (COR1 and COR2) and two heliospheric imagers (HI1 and HI2) on board the *STEREO* mission. The in situ *PSP* measurements from rapidly varying heliocentric distances will record the spatio-temporal variance of large-scale solar wind streams. The large-scale context of the ambient structures around *PSP* could be further resolved in the longitudinal dimension, using additional WL imagery from *SolO*, from an OOE perspective. Coordinated observations between *PSP* and *SolO* are very promising in enabling background CIRs and transient ejecta to be differentiated, and for uncovering the 3D structures and distribution of quiescent large-scale solar wind streams.
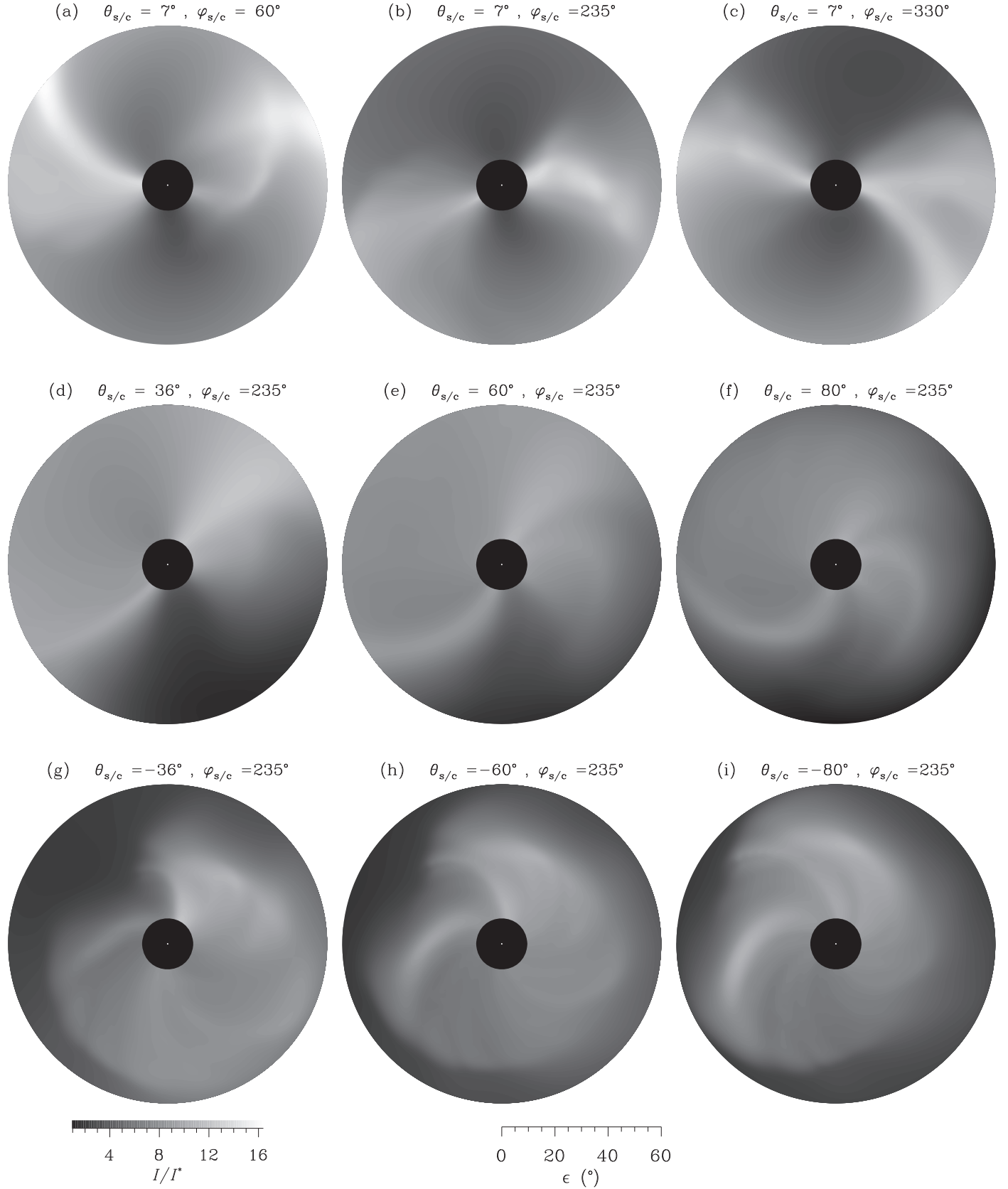
15

White−Light Sky Map Viewed from an Imager at $r_{\mathrm{s/c}} = 60\ R_\odot$

(a) $\theta_{\mathrm{s/c}} = 7°$, $\varphi_{\mathrm{s/c}} = 60°$ (b) $\theta_{\mathrm{s/c}} = 7°$, $\varphi_{\mathrm{s/c}} = 235°$ (c) $\theta_{\mathrm{s/c}} = 7°$, $\varphi_{\mathrm{s/c}} = 330°$

(d) $\theta_{\mathrm{s/c}} = 36°$, $\varphi_{\mathrm{s/c}} = 235°$ (e) $\theta_{\mathrm{s/c}} = 60°$, $\varphi_{\mathrm{s/c}} = 235°$ (f) $\theta_{\mathrm{s/c}} = 80°$, $\varphi_{\mathrm{s/c}} = 235°$

(g) $\theta_{\mathrm{s/c}} = -36°$, $\varphi_{\mathrm{s/c}} = 235°$ (h) $\theta_{\mathrm{s/c}} = -60°$, $\varphi_{\mathrm{s/c}} = 235°$ (i) $\theta_{\mathrm{s/c}} = -80°$, $\varphi_{\mathrm{s/c}} = 235°$

I/I^* $\epsilon\ (°)$

Figure 13. Normalized WL brightness I/I^* of the heliosphere over the elongation range $\varepsilon \in [8°,\ 60°]$, as imaged from a number of viewpoints as prescribed in Figure 12.

Our understanding of solar transients (i.e., CMEs, solar flares, energetic particles), and their impact on the heliosphere, has advanced greatly in the last decade, enabled by multi-spacecraft observations and high-performance numerical MHD simulations. These transients, at a small scale near the Sun and at a larger scale between Sun and 1 au, are now routinely observed by both remote-sensing and in situ instruments on space-borne observatories. Numerical MHD simulations of the corona and heliosphere have advanced rapidly over the same time frame, allowing data-driven modeling of realistic events and real-time prediction. The improved numerical models and new analysis tools should ideally be developed within, for example, the framework of the Community Coordinated Modeling Center (https://ccmc.gsfc.nasa.gov) to maximize the exploitation of the novel data that will be provided by these new missions including *PSP* and *SolO*. A consistent approach to be the assimilation of observational and modeling data in the unprecedented *PSP–SolO* era would enable rigorous tests of the various theories proposed to explain how solar activity drives heliospheric variability. As predicted by the forward modeling results presented in this paper, the WL imagers on board the OOE *SolO* spacecraft will provide context for in situ and remote-sensing observations by the in-ecliptic *PSP* spacecraft, and such synergies between *SolO* and *PSP* can deconvolve the spatio-temporal variability of large-scale solar wind streams.

ORCID iDs

Ming Xiong ● https://orcid.org/0000-0001-9427-7366
Jackie A. Davies ● https://orcid.org/0000-0001-9865-9281
Xueshang Feng ● https://orcid.org/0000-0001-8605-2159
Bo Li ● https://orcid.org/0000-0003-4790-6718
Lidong Xia ● https://orcid.org/0000-0001-8938-1038
Richard A. Harrison ● https://orcid.org/0000-0002-0843-0845
Keiji Hayashi ● https://orcid.org/0000-0001-9046-6688
Huichao Li ● https://orcid.org/0000-0002-1732-0196

References

Abbo, L., Ofman, L., Antiochos, S. K., et al. 2016, SSRv, 201, 55
Akioka, M., Nagatsuma, T., Miyake, W., Ohtaka, K., & Marubashi, K. 2005, AdSpR, 35, 65
Appourchaux, T., Auchère, F., Antonucci, E., et al. 2014, SOLARIS: SOLAR Sail Investigation of the Sun, ed. M. Macdonald, (Berlin: Springer), 259
Biesecker, D. A., Reinard, A., Cash, M. D., et al. 2015, AGU Fall Meeting, SH12A-06
Biesecker, D. A., Webb, D., & Cyr, O., St. 2008, SSRv, 136, 45
Billings, D. E. 1966, A Guide to the Solar Corona (New York: Academic Press)
Borovsky, J., & Denton, M. 2010, JGRA, 115, 10101
Cranmer, S. R., Gibson, S. E., & Riley, P. 2017, SSRv, 212, 1345
Davies, J. A., Harrison, R. A., Perry, C. H., et al. 2012, ApJ, 750, 23
Davies, J. A., Harrison, R. A., Rouillard, A. P., et al. 2009, GeoRL, 36, L02102
Davis, C. J., Davies, J. A., Lockwood, M., et al. 2009, GeoRL, 36, L08102
DeForest, C. E., Howard, T. A., & McComas, D. J. 2013, ApJ, 769, 43
DeForest, C. E., Howard, T. A., & McComas, D. J. 2014, ApJ, 787, 124
Domingo, V., Fleck, B., & Poland, A. I. 1995, SSRv, 72, 81
Eyles, C. J., Harrison, R. A., Davis, C. J., et al. 2009, SoPh, 254, 387
Eyles, C. J., Simnett, G. M., Cooke, M. P., et al. 2003, SoPh, 217, 319
Feng, X., Yang, L., Xiang, C., et al. 2010, ApJ, 723, 300
Fox, N. J., Velli, M. C., Bale, S. D., et al. 2016, SSRv, 204, 7
Gopalswamy, N., Davila, J. M., Cyr, O. C., St., et al. 2011, JASTP, 73, 658
Gosling, J. T. 1990, GMS, 58, 343
Gosling, J. T., Bame, S. J., McComas, D. J., et al. 1993, GeoRL, 20, 2789
Harrison, R. A., Davis, C. J., Eyles, C. J., et al. 2008, SoPh, 247, 171
Holzer, T. E. 1989, ARA&A, 27, 199
Howard, R. A., Moses, J. D., Vourlidas, A., et al. 2008, SSRv, 136, 67
Howard, T. A., & DeForest, C. E. 2012, ApJ, 752, 130
Howard, T. A., & Tappin, S. J. 2009, SSRv, 147, 31
Hundhausen, A. J. 1993, JGR, 98, 13
Jackson, B., Buffington, A., Hick, P., Bisi, M., & Clover, J. 2010, SoPh, 265, 257
Jackson, B. V., & Leinert, C. 1985, JGR, 90, 10759
Kaiser, M. L., Kucera, T. A., Davila, J. M., et al. 2008, SSRv, 136, 5
Kraft, S., Puschmann, K. G., & Luntama, J. P. 2017, Proc. SPIE, 10562, 105620F
Kuznetsov, V. D., Zelenyi, L. M., Zimovets, I. V., et al. 2016, Ge&Ae, 56, 781
Lavraud, B., Liu, Y., Segura, K., et al. 2016, JASTP, 146, 171
Leer, E., & Holzer, T. E. 1980, JGR, 85, 4681
Leer, E., Holzer, T. E., & Fla, T. 1982, SSRv, 33, 161
Leinert, C., & Pitz, E. 1989, A&A, 210, 399
Lepping, R. P., Acúña, M. H., Burlaga, L. F., et al. 1995, SSRv, 71, 207
Liewer, P. C., Ayon, J., Alexander, D., et al. 2008, in Solar Polar Imager: Observing Solar Activity from a New Perspective, ed. M. S. Allen (Reston, VA: American Institute of Aeronautics and Astronautics), 1
Liu, Y., Davies, J. A., Luhmann, J. G., et al. 2010, ApJL, 710, L82
McComas, D. J., Barraclough, B. L., Funsten, H. O., et al. 2000, JGR, 105, 10419
Muller, D., Marsden, R. G., Cyr, O. C., St, & Gilbert, H. R. 2013, SoPh, 285, 25
Neugebauer, M., & Snyder, C. W. 1966, JGR, 71, 4469
Neugebauer, M., & Snyder, C. W. 1967, JGR, 72, 1823
Rouillard, A. P., Davies, J. A., Forsyth, R. J., et al. 2008, GeoRL, 35, L10110
Schwadron, N. A., Connick, D. E., & Smith, C. 2010, ApJL, 722, L132
Schwenn, R., Montgomery, M. D., Rosenbauer, H., et al. 1978, JGR, 83, 1011
Sheeley, N. R., Jr., Herbst, A. D., Palatchi, C. A., et al. 2008, ApJ, 674, 109
Smith, E. J., Marsden, R. G., & Page, D. E. 1995, Sci, 268, 1005
Stone, E. C., Frandsen, A. M., Mewaldt, R. A., et al. 1998, SSRv, 86, 1
Suess, S. T. 1990, RvGeo, 28, 97
Tousey, R. 1973, in Space Research Conf. 2, ed. M. J. Rycroft & S. K. Runcorn (Berlin: Akadmie Verlag), 713
Tu, C.-Y., Zhou, C., Marsch, E., et al. 2005, Sci, 308, 519
Vourlidas, A., & Howard, R. A. 2006, ApJ, 642, 1216
Vourlidas, A., Howard, R. A., Plunkett, S. P., et al. 2016, SSRv, 204, 83
Wang, Y.-M., & Sheeley, N. R., Jr. 1990, ApJ, 355, 726
Webb, D. F., & Howard, R. A. 1994, JGR, 99, 4201
Wenzel, K. P., Marsden, R. G., Page, D. E., & Smith, E. J. 1992, A&AS, 92, 207
Wu, J., Sun, W. Y., Zheng, J. H., et al. 2011, AdSpR, 48, 943
Xiong, M., Davies, J. A., Bisi, M. M., et al. 2013a, SoPh, 285, 369
Xiong, M., Davies, J. A., Feng, X., et al. 2013b, ApJ, 777, 32
Xiong, M., Davies, J. A., Harrison, R. A., et al. 2018, ApJ, 852, 111
Xiong, M., Davies, J. A., Li, B., et al. 2017, ApJ, 844, 76
Xiong, M., Liu, Y., Liu, H., et al. 2016, ChJSS, 36, 245
Yang, L. P., Feng, X. S., Xiang, C. Q., et al. 2012, JGR, 117, A08110